

Article

Improved Line Intensity Analysis of Neutral Helium by Incorporating the Reabsorption Processes in a Helium Collisional-Radiative Model

Keren Lin ¹, Motoshi Goto ²  and Hiroshi Akatsuka ^{3,*} 

¹ Department of Electronic and Electrical Engineering, Tokyo Institute of Technology, Tokyo 152-8550, Japan; lin.k.ac@m.titech.ac.jp

² National Institute for Fusion Science, Toki 509-5292, Japan; goto.motoshi@nifs.ac.jp

³ Institute of Innovative Research, Tokyo Institute of Technology, Tokyo 152-8550, Japan

* Correspondence: hakatsuk@zic.iir.titech.ac.jp

Abstract: In this study, eight emission lines in the visible wavelength range of neutral helium were used to diagnose the electron density and temperature of the Large Helical Device (LHD) helium plasma instead of the conventional three-line method. The collisional-radiative (CR) model for low-pressure helium plasma was revised to include the optical escape factors for spontaneous transition from the n^1P states to the ground state so that the influence of the absorption effect under optically thick conditions could be considered. The developed algorithm was based on fitting the number densities of eight excited states obtained using optical emission spectroscopy (OES). The electron density, electron temperature, ground-state density, and optical escape factors were selected as the fitting parameters. The objective function was set as the summation of the residual errors between the number densities measured in the experiment and those calculated using the revised model. A regularization term was introduced for the optical escape factor and optimized through bias and variance analyses. The results show that the agreement between the number density calculated by the algorithm and its counterpart measured in the experiment was generally improved compared to the method using three lines.

Keywords: absorption effect; CR model; OES measurement; optical escape factor



Citation: Lin, K.; Goto, M.; Akatsuka, H. Improved Line Intensity Analysis of Neutral Helium by Incorporating the Reabsorption Processes in a Helium Collisional-Radiative Model. *Atoms* **2023**, *11*, 94. <https://doi.org/10.3390/atoms11060094>

Academic Editor: Mohammed Koubiti

Received: 29 March 2023

Revised: 31 May 2023

Accepted: 6 June 2023

Published: 8 June 2023



Copyright: © 2023 by the authors. Licensee MDPI, Basel, Switzerland. This article is an open access article distributed under the terms and conditions of the Creative Commons Attribution (CC BY) license (<https://creativecommons.org/licenses/by/4.0/>).

1. Introduction

Currently, optical emission spectroscopy (OES) measurement is generally used to acquire plasma parameters. Because it does not require direct contact with the plasma, this method is relatively more effective and safer than other applicable methods and is capable of measuring the plasma parameters under different conditions, such as low-pressure microwave-induced plasma [1], atmospheric pressure non-equilibrium plasma [2], and Large Helical Device (LHD) plasma [3]. OES diagnoses employing the collisional-radiative (CR) model are used to diagnose the electron density and temperature of different types of gases [4,5].

Emission lines in the visible wavelength range are widely used for plasma diagnosis. Three-line diagnosis is commonly used to diagnose the electron density and temperature of helium plasmas. This method is relatively safe and effective because it requires the measurement of only three lines in the visible wavelength range; however, the results are sometimes inconsistent with other diagnostic results. Therefore, the conventional method requires further improvements to enhance its reliability.

For plasmas with lower electron temperatures, the performance of the line intensity ratio (LIR) method and laser Thomson scattering (LTS) method has been investigated for recombining detached plasmas [6]. Additionally, the optical escape factor in cylindrical geometries has been calculated and applied to weakly ionized helium using the CR model [7,8].

However, the escape factor for helium plasmas with high electron temperatures in LHD has not yet been studied.

In this study, the CR model developed by Goto [9] and Fujimoto [10] was revised. The model considers 65 discrete energy levels of neutral helium, including one ground state (1^1S) and 64 excited states ($2 \leq n \leq 26$). Each L (orbital angular momentum quantum number) level with n (principal quantum number) less than or equal to seven is considered independently, except for levels with L greater than or equal to three. These specific levels with $L \geq 3$ are combined into a single level. For levels with n between 8 and 10, the different L levels are grouped together. Levels with n greater than or equal to 11 are approximated using hydrogenic levels that possess statistical weights twice as those of hydrogen. It has all the fundamental electron collisions and radiation processes for low-pressure helium plasmas. Particularly, it considers electron collision excitation and de-excitation, electron collision ionization, electron three-body recombination, spontaneous transitions, and di-electronic and radiative recombination. The corresponding rate coefficients were obtained using the equations presented in Refs. [11–14].

This study demonstrates a new algorithm for determining the electron density and temperature of helium plasma. Section 2 demonstrates that the conventional method, which uses only three emission lines, exhibits inconsistencies seen in the results. Section 3 illustrates the revision of the CR model and the development of the algorithm. Sections 4 and 5 present relevant experiments, discussions, and conclusions, respectively.

2. Experiment

The measurements were performed for the LHD, which is a heliotron-type experimental device for magnetically confined fusion plasmas. We measured the spectra for 10 discharges with helium gas, for which the magnetic axis radius was fixed at 3.6 m, while the magnetic field strength was changed to 0.75, 1.5, and 2.75 T. The line-of-sight was roughly in the radial direction, passing through the central plasma region on a horizontally elongated poloidal cross-section, as shown in Figure 1.

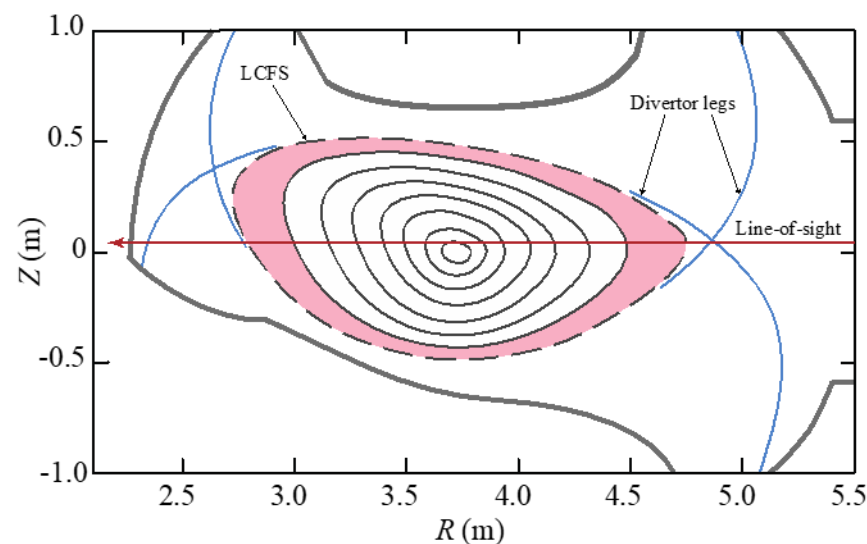


Figure 1. A cross-sectional view of the plasma with magnetic flux surfaces in the measurement.

The field view collimated by the lens had an approximately 30 mm wide cylindrical profile. The light introduced into an optical fiber with a core diameter of 100 μm was guided to a Czerny-Turner type spectrometer with a focal length of 0.5 m. The spectrometer was equipped with a grating of 100 grooves/mm, and the reciprocal linear dispersion was measured to be 19.976 nm/mm. We used a charge-coupled device (CCD) consisting of 1024 pixels \times 255 pixels, with each pixel measuring 26 μm \times 26 μm , as the detector. Consequently, a wavelength of approximately 520 nm could be measured simultaneously.

The central wavelength was adjusted to cover all six transitions from $n = 3$ to $n = 2$, i.e., from 388.9 nm to 728.1 nm. The absolute sensitivity of the entire system was calibrated using a standard light source, which consisted of a halogen lamp and an integrated sphere (Labsphere USS-600C). The radiance ($\text{W}\cdot\text{m}^{-2}\cdot\text{nm}^{-1}\cdot\text{sr}^{-1}$) at the aperture of the integrated sphere was known, and we derived the radiance of the plasma by comparing the signal counts at the actual measurement and at the calibration measurement. We collected the data for 12 discharges under various plasma conditions. Each discharge typically lasted for 2 s, and spectra were recorded every 5 min.

An example of the measured spectra is shown in Figure 2.

Table 1. Helium lines used in the line spectrum analysis.

Wavelength $\lambda_{p,q}$ (nm)	Transition ($n^{2S+1}L \rightarrow n'^{2S'+1}L'$)	$A_{p,q}$ (s^{-1})
728.135	$3^1S \rightarrow 2^1P$	1.8291×10^7
706.525	$3^3S \rightarrow 2^3P$	2.7849×10^7
501.568	$3^1P \rightarrow 2^1S$	1.3368×10^7
388.864	$3^3P \rightarrow 2^3S$	0.9472×10^7
667.815	$3^1D \rightarrow 2^1P$	6.3676×10^7
587.566	$3^3D \rightarrow 2^3P$	7.0693×10^7
492.193	$4^1D \rightarrow 2^1P$	1.9855×10^7
447.150	$4^3D \rightarrow 2^3P$	2.4574×10^7

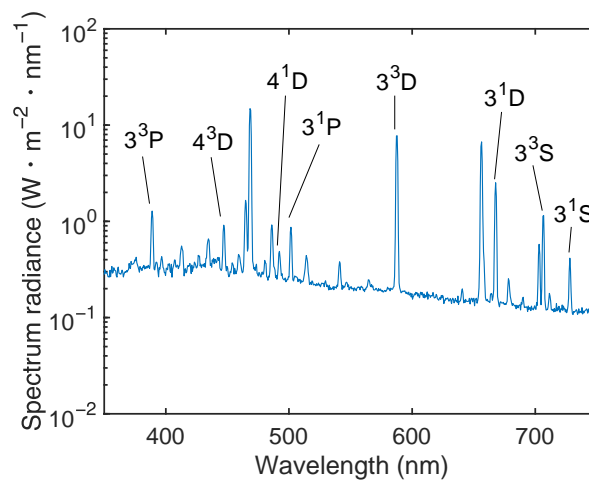


Figure 2. Spectra of the LHD helium plasma in the visible wavelength range. The designations indicate the upper levels of the transitions, while the corresponding lower levels are shown in Table 1.

Eight emission lines corresponding to neutral helium were identified. In LHD, it is known that neutral helium line emissions are localized in a thin layer at the plasma edge region [15]. Therefore, the local T_e and n_e values at the line emission location could be diagnosed through an analysis of the spectra. In this study, the selected lines for diagnosis were not optically thick and were not subjected to the reabsorption effect. The line-integrated number density of the upper level of the corresponding spontaneous transition is determined as follows:

$$n_p = \frac{\lambda_{p,q} \Phi_{p,q}}{hc A_{p,q}} \tag{1}$$

where h is Planck’s constant, c is the speed of light, $\lambda_{p,q}$ is the photon wavelength of the corresponding transition, $A_{p,q}$ is Einstein’s A coefficient, and $\Phi_{p,q}$ ($\text{W}\cdot\text{m}^{-2}$) is the line-integrated spectral flux density, which was obtained by integrating the spectral radiance $L(\lambda)$ ($\text{W}\cdot\text{m}^{-2}\cdot\text{nm}^{-1}\cdot\text{sr}^{-1}$) over the corresponding emission line:

$$\Phi_{p,q} = 4\pi \int_{\text{line}} L(\lambda) d\lambda. \tag{2}$$

Table 1 lists the parameters of the emission lines examined. A conventional three-line diagnosis for deriving T_e and n_e was first attempted using three emission lines, i.e., 667.8 nm, 706.5, and 728.1 nm [15]. The results are shown in Figure 3. The red and blue symbols in Figure 3a represent the intensity ratios of the specific lines for the diagnosis plotted against the line-averaged electron density. The line-averaged electron density was calculated by dividing the line-integrated density measured by an interferometer by the plasma length. This measurement provided information about the entire plasma, including the core region. On the other hand, helium line emissions were localized at the plasma edge. As a result, it is generally expected that the electron density derived from these emissions will be lower than the line-averaged electron density.

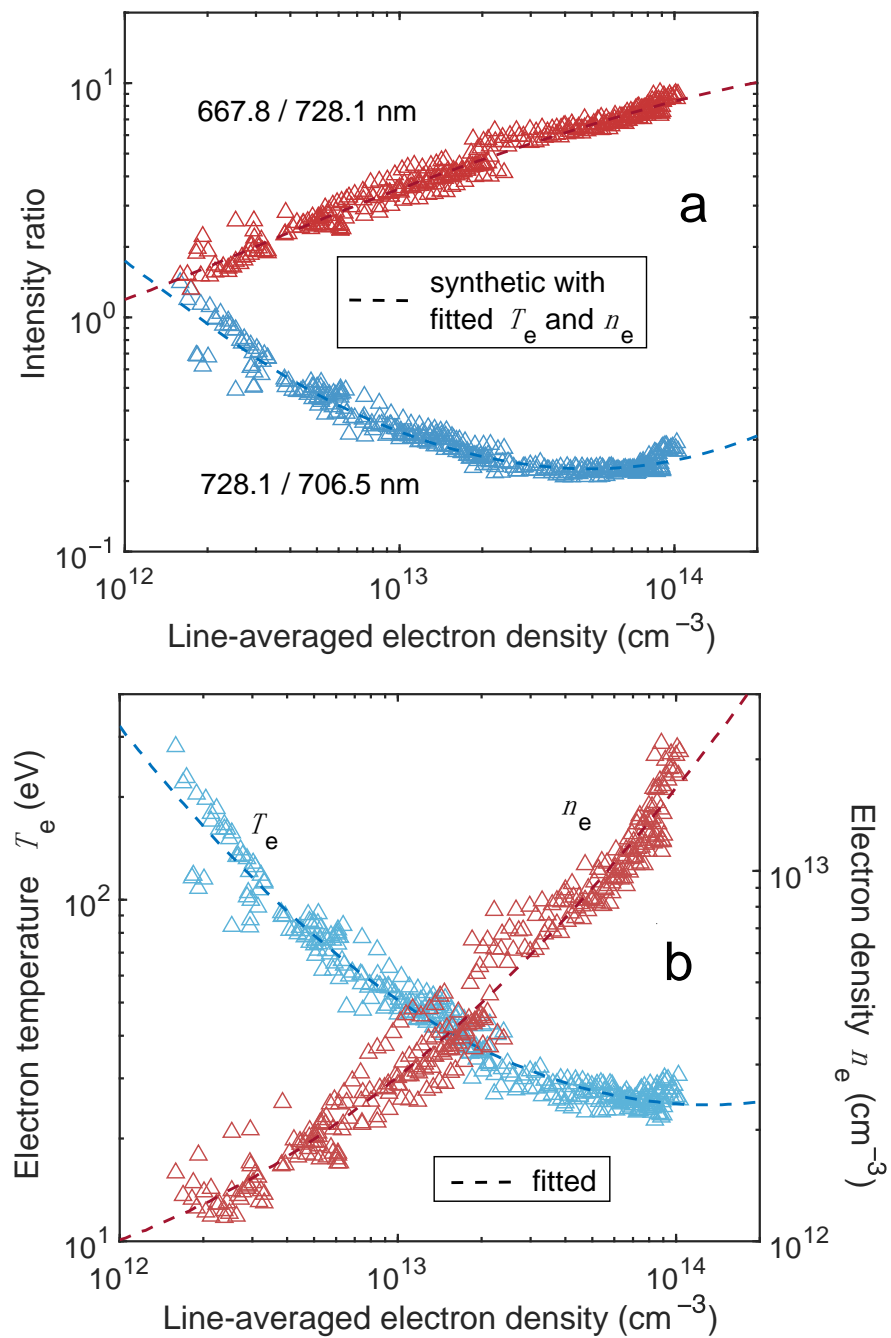


Figure 3. Cont.

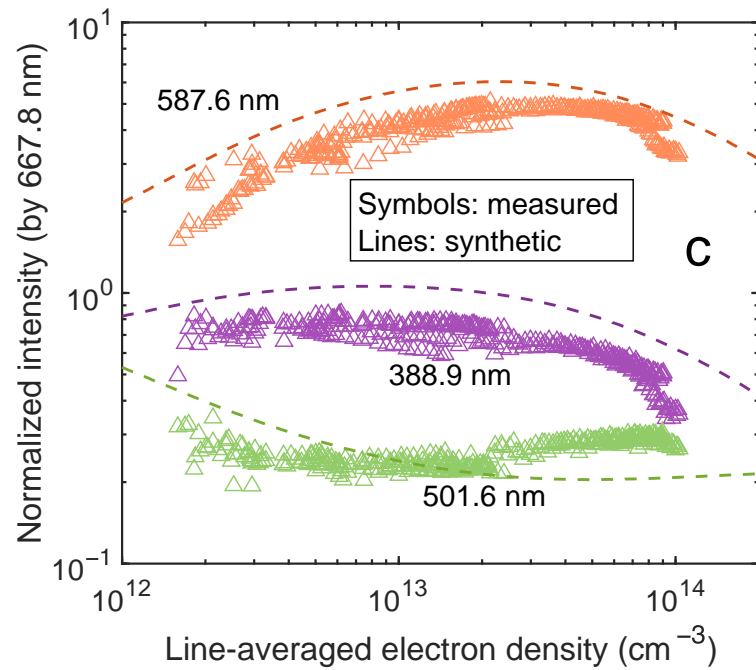


Figure 3. Results obtained with three emission lines: (a) intensity ratio of three lines for diagnosis, (b) electron density and temperature diagnosed via the three-line diagnosis, (c) comparison between the normalized intensities fitted by three-line diagnosis and their counterparts measured via OES method directly. The triangles represent the data obtained using the OES method.

The parameters T_e and n_e were determined by minimizing the function as follows:

$$f(T_e, n_e) = \sum_p \left(\frac{n_p - n'_p}{n_p} \right)^2 \tag{3}$$

where n_p is the measured number density, and n'_p was calculated using the CR model with the given T_e and n_e . The corresponding electron densities and temperatures are indicated by the red and blue symbols in Figure 3b, respectively. The diagnosed electron density increased with the increase in the line-averaged electron density \bar{n}_e , and the electron temperature decreased. The changes in electron density and temperature relative to the line-averaged electron density showed similar trends to the changes in the 667.8/728.1 nm and 728.1/706.5 nm line ratios relative to the line-averaged electron density, respectively. This three-line method for determining the electron density and temperature was first suggested by Schweer et al. [16]. The results were fitted with polynomial functions, and they are shown as dashed lines. The synthetic intensity ratios (dashed lines) obtained using the fitted T_e , n_e , and CR model [17] are shown in Figure 3a with the dashed lines. The synthetic results for the intensity ratios of the three lines agreed well with their original values, as shown in Figure 3a.

We examined the results obtained using emission lines that were not used for T_e and n_e determinations. The intensities of the three lines (from $n = 3$ to $n = 2$, normalized by the 667.8 nm line intensity) obtained via the OES measurement were compared with the synthetic results shown in Figure 3c. Some disagreements can be observed, i.e., the synthetic results of the lines at 388.9 and 587.6 nm have tendencies similar to the corresponding measured results; however, constant differences in the results (lines and symbols) exist. In addition, the measured results of the line at 501.6 nm show a trend opposite to that of the corresponding synthetic result. We suspect that the reabsorption effects of the transition 3^1P-1^1S , which has the same upper level as the line at 501.6 nm, could be causing this. Thus, it can be considered that using three lines to diagnose the electron density and

temperature with the OES measurement and CR model cannot perfectly fit the measured results. Conventional diagnoses can be further improved.

3. Model Extension

3.1. Optical Escape Factor

At an earlier time, Kajita et al. investigated radiation trapping by additionally measuring one or two specific lines. The escape factors for the spontaneous transition from 2^1P , 3^1P , 4^1P , and 5^1P states to the ground state have been evaluated in general cases [18]. In this study, the reabsorption effect in LHD was incorporated into the model as an escape factor. An accurate evaluation of the escape factor is generally difficult. In a previous study, the escape factor was considered the fitting parameter [17]. However, the escape factor was introduced only for a single resonance line (1^1S-4^1P), and the validity of the obtained value was not examined. Thus, we developed a method to determine the fitting conditions for the escape factors. The escape factors can be evaluated by assuming that the plasma has a slab or a cylindrical structure. Iida suggested a complete analytic expression for the optical escape factor in a cylindrical geometry [19]. For LHD helium plasma, in a previous study, we found that the line emissions of neutral helium are localized within a layer of thickness in the order of 1 cm at the plasma boundary, whereas the minor radius of the plasma is in the order of 1 m [15]. Because the line-of-sight of the present measurement is almost perpendicular to the emission layer, we believe that the situation can be approximated by a slab model. In addition, the precise plasma geometry is not well understood, and it is difficult to accurately calculate the theoretical escape factor. Instead, we can use it as a fitting parameter and use the calculated theoretical value as a constraint. Thus, an infinite plane-parallel slab model [20] with a thickness of $D = 0.01$ m was applied. The optical escape factor at the center of the slab is expressed as follows:

$$\Lambda_{p,q} = \int_0^1 T\left(\frac{\kappa D}{2x}\right) dx \tag{4}$$

where x is the cosine of the inclination of the z -axis in Ref. [20], κ is the absorption coefficient [16] which can be obtained as follows:

$$\kappa = \frac{e^2}{4\epsilon_0 m_e c} n_q f_{q,p} P(\nu) \tag{5}$$

where $P(\nu)$, ϵ_0 , m_e , e , and $f_{q,p}$ are the line profile, vacuum permittivity, mass of the electron, elementary charge, and oscillator strength, respectively. The Doppler profile [21,22] is used for calculating the line profile $P(\nu)$. It is expressed as follows:

$$P(\nu) d\nu = \frac{1}{\sqrt{\pi} \Delta\nu_D} \exp\left[-\left(\frac{\nu - \nu_0}{\Delta\nu_D}\right)^2\right] d\nu \tag{6}$$

with the Doppler width

$$\Delta\nu_D = \frac{\nu_0}{c} \sqrt{\frac{2k_B T_g}{m_{He}}} \tag{7a}$$

and the central frequency

$$\nu_0 = \frac{\epsilon_p^{ex} - \epsilon_q^{ex}}{h} \tag{7b}$$

where k_B , T_g , and m_{He} are the Boltzmann's constant, gas temperature, and mass of the helium atom, respectively. ϵ_p^{ex} and ϵ_q^{ex} are the excitation energies of levels p and q , respectively. $T(\tau_0)$ is the average probability that a photon within the line profile propagates τ_0 :

$$T(\tau_0) = \int_{-\infty}^{\infty} \exp\left[-\tau_0 \frac{P(\nu)}{P(0)}\right] P(\nu) d\nu \tag{8}$$

Figure 4 shows the calculated optical escape factors for the levels n^1P as a function of the ground-state density.

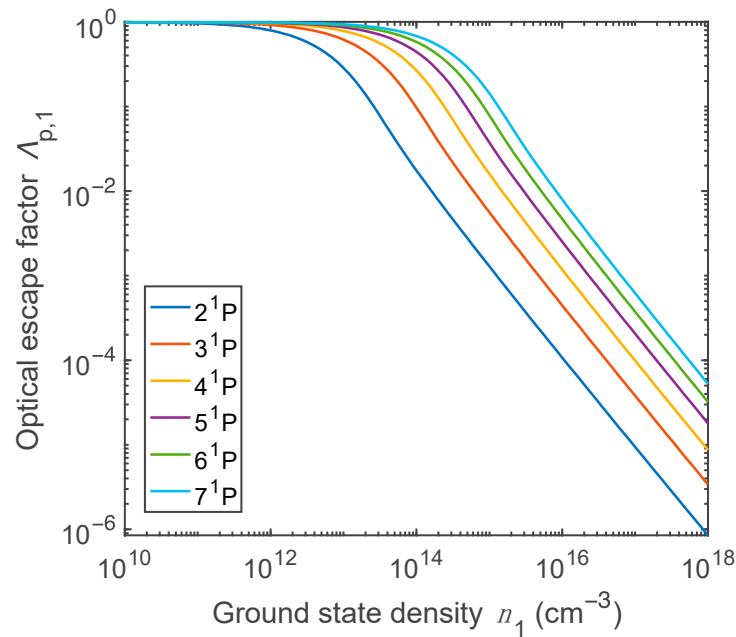


Figure 4. Optical escape factor for the n^1P levels ($n = 2, 3, 4, 5, 6,$ and 7).

Level 2^1P exhibited the lowest optical escape factor among the six n^1P levels. This indicates that lower levels have a relatively stronger absorption effect. The absorption effect of n^1P ($n = 5, 6,$ and 7) can be neglected when the ground-state density is lower than 10^{13} cm^{-3} . In the revised CR model, we used the following equation to calculate the depopulating flux contributed by a spontaneous transition in the rate equation:

$$\Gamma_{p,q}^{\text{rad}} = \Lambda_{p,q} A_{p,q} n_p \tag{9}$$

where $\Lambda_{p,q}$ is set to 1 for optically thin states. This is the same technique employed in Ref. [8].

3.2. Bias–Variance Analysis

An algorithm for diagnosing the electron density and temperature was developed in this study. We evaluated the escape factors with a slab structure; the fitting was conducted with the restriction that the derived escape factors should not differ significantly from the evaluated escape factors. This restriction can be realized using a regularization term in the object function

$$f_{\text{obj}} = \sum_p \left(\frac{n_p - n'_p}{n_p^{\text{small}}} \right)^2 + \mu \left(\frac{\Lambda_{n^1P,1^1S}^{\text{cal}} - \Lambda'_{n^1P,1^1S}}{\Lambda_{n^1P,1^1S}^{\text{cal}}} \right)^2 \tag{10}$$

where $\Lambda'_{n^1P,1^1S}$ is the escape factor generated by the optimizing algorithm. n_p^{small} denotes the smaller one among n_p and n'_p . $\Lambda_{n^1P,1^1S}^{\text{cal}}$ is the optical escape factor calculated using Equation (4), which is a function of n'_1 when T_g and D are fixed. The hyperparameter μ controls the weight of restriction of the escape factors. A schematic of the fitting algorithm is shown in Figure 5.

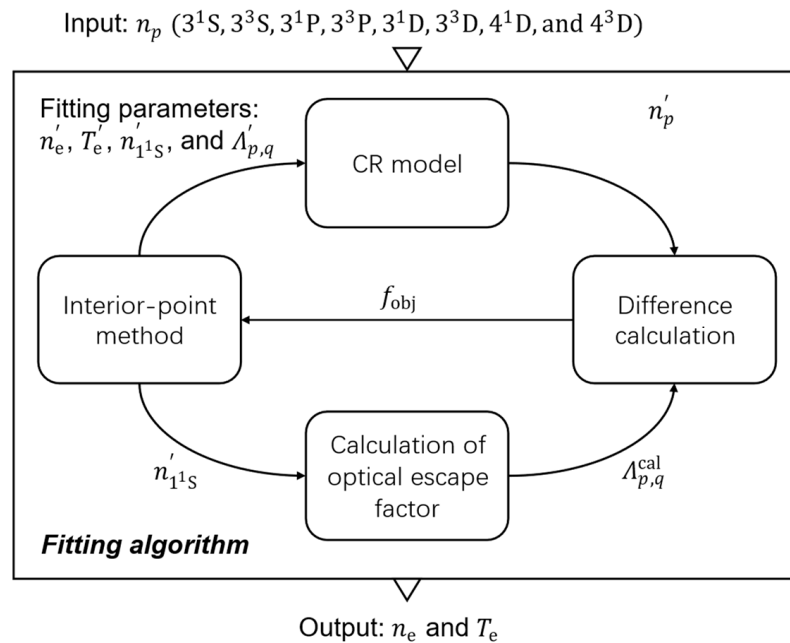


Figure 5. Fitting algorithm for diagnosing the electron density and temperature.

The algorithm employs the number of densities corresponding to the eight measured emission lines as inputs. The interior point method [23,24] is applied to optimize the object function. The optimizing algorithm generates n'_e , T'_e , n'_{1^1S} , and $\Lambda'_{p,q}$ with different values and determines the global minimum of the object function. The outputs are n'_e and T'_e , which minimize the object function. An optimum value of μ is determined via bias–variance analysis [25–27]. The analysis helps us understand the trade-off between the new model’s ability to fit the measured line intensity well (low bias) and its ability to generalize accurate electron density, electron temperature, ground-state density, and escape factors (low variance). By analyzing the bias and variance of the new model, we made informed decisions about parameter selection and complexity to achieve better performance. In the bias–variance analysis, additional measurements have been taken. The helium plasma is generated under stable conditions. In total, 40 spectra are obtained from the OES measurements every 0.01 s. It is assumed that the electron density and temperature are constant during the 0.4 s. The acquired spectra are used for analysis. The bias is obtained as follows:

$$(bias)^2 = \frac{1}{8} \sum_p \left[\frac{\log_{10} \left(\left| \bar{n}_p^{meas} - \bar{n}_p^{fit} \right| \right)}{\log_{10} \left(\bar{n}_p^{meas} \right)} \right]^2 \tag{11}$$

and the variance “var” is obtained by the following:

$$var = \frac{1}{8} \sum_p \left\{ \frac{1}{K} \sum_{k=1}^K \left[\frac{\log_{10} \left(\left| \bar{n}_p^{fit} - n_p^{(k)fit} \right| \right)}{\log_{10} \left(\bar{n}_p^{fit} \right)} \right]^2 \right\}, \tag{12}$$

where \bar{n}_p^{meas} is the mean value of the measured number density of level p , \bar{n}_p^{fit} is the mean value of the number density obtained via the fitting algorithm, and $n_p^{(k)fit}$ is the fitted number density of level p in the k -th measured spectrum. This bias expresses the discrepancy between the fitted results and measurements. The variance corresponds to the degree of variation in the fitted results under approximately identical plasma conditions. The bias and variance with different μ , in the range of 0.01–100, are shown in Figure 6.

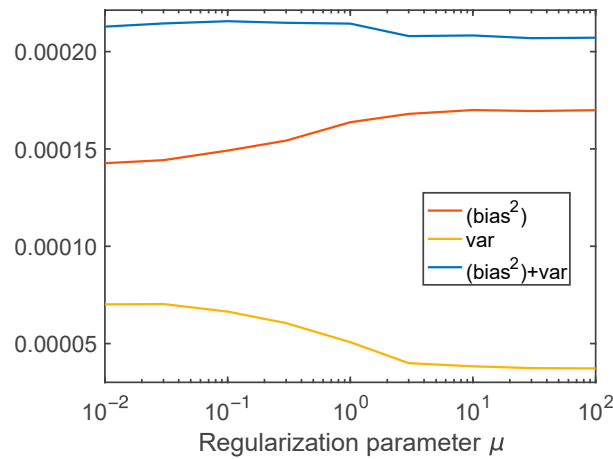


Figure 6. Calculated bias and variance of the algorithm with different μ .

The bias increases with an increase in the regularization parameter; it is relatively steady when μ is higher than 3. The variance also decreases rapidly when μ is lower than 3 and is steady when μ is higher than 3. This indicates that the algorithm can be overfitted when $\mu < 3$. It is difficult to determine the global minimum of the total error; however, $\mu = 5$ is considered reasonable in the present case. It restricts the optical escape factors generated by the algorithm within a reasonable range but is not completely a function of the ground-state density.

The present model could still suffer from an overfitting problem, and we attempted to optimize the number of escape factors considered in the model. We conducted a bias–variance analysis by increasing the number of escape factors considered in the model. The used fitting parameters and results are shown in Table 2 and Figure 7, respectively.

Table 2. Fitting parameters used in bias–variance analysis.

Number of Fitting Parameters	Fitting Parameter
3	n_e, T_e, n_{1S}
4	$n_e, T_e, n_{1S}, \Lambda_{2^1P,1^1S}$
5	$n_e, T_e, n_{1S}, \Lambda_{2^1P,1^1S}, \Lambda_{3^1P,1^1S}$
6	$n_e, T_e, n_{1S}, \Lambda_{2^1P,1^1S}, \Lambda_{3^1P,1^1S}, \Lambda_{4^1P,1^1S}$
7	$n_e, T_e, n_{1S}, \Lambda_{2^1P,1^1S}, \Lambda_{3^1P,1^1S}, \Lambda_{4^1P,1^1S}, \Lambda_{5^1P,1^1S}$
8	$n_e, T_e, n_{1S}, \Lambda_{2^1P,1^1S}, \Lambda_{3^1P,1^1S}, \Lambda_{4^1P,1^1S}, \Lambda_{5^1P,1^1S}, \Lambda_{6^1P,1^1S}$

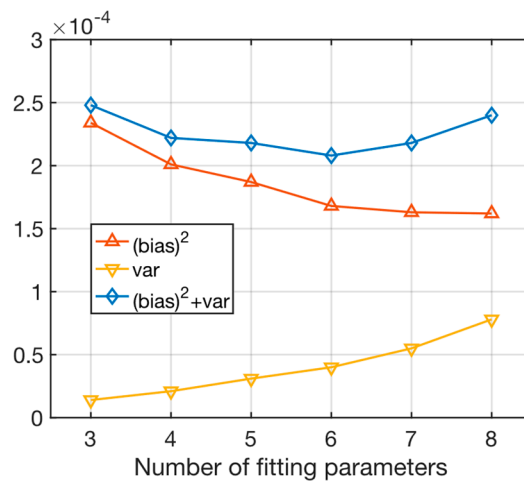


Figure 7. Calculated bias and variance of the algorithm with different numbers of the fitting parameters.

The variance increases steadily with an increase in the number of fitting parameters. The bias decreases rapidly when the number of fitting parameters is less than six. The minimum total error was recorded when the number of fitting parameters was six. Therefore, six parameters (n_e , T_e , n_1 , $\Lambda_{2^1P,1^1S}$, $\Lambda_{3^1P,1^1S}$, and $\Lambda_{4^1P,1^1S}$) were selected as the fitting parameters for the algorithm.

4. Results and Discussion

We conducted fitting using the model described in Section 2 for the line intensity data shown in Figure 2. The electron densities and temperatures diagnosed are shown in Figure 8.

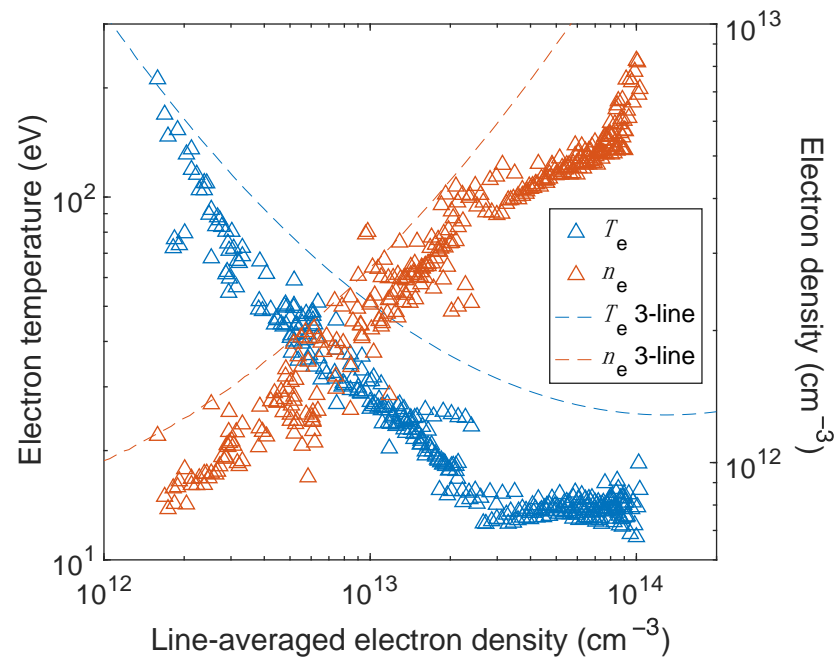


Figure 8. Electron density and temperature obtained using the novel fitting algorithms (symbols and dashed lines represent results obtained using the new model and three-line analysis, respectively).

Both the electron density and temperature obtained using the novel method showed increasing and decreasing tendencies, respectively, with an increase in the line-averaged electron density, which was similar to the results obtained using the three-line method, as shown in Figure 3b. When the line-averaged electron density was low, the electron temperatures obtained using the two methods were similar. The electron temperature diagnosed using the new model decreased faster when the line-averaged electron density increased. The electron density obtained using the proposed model was generally slightly lower than that obtained using the three-line method.

A comparison of the normalized line intensities is shown in Figure 9. An example of line spectra reproduced by the new model and three-line analysis is shown in Figure 10. Compared to the three-line method, the difference between the fitted and measured results for the 706.5 and 728.1 nm lines increased slightly. A relatively large difference appeared when the line-averaged electron density was higher than $2 \times 10^{13} \text{ cm}^{-3}$. The fitting of the 501.6 and 587.6 nm lines improved when the line-averaged electron density was between 10^{12} and $2 \times 10^{13} \text{ cm}^{-3}$. When the line-averaged electron density was higher than $2 \times 10^{13} \text{ cm}^{-3}$, the 501.6 nm line had a relatively better fitting. For the 447.2 and 492.2 nm lines, the difference between the measured and fitted results improved. In general, the results fitted with the new model exhibited relatively better performance.

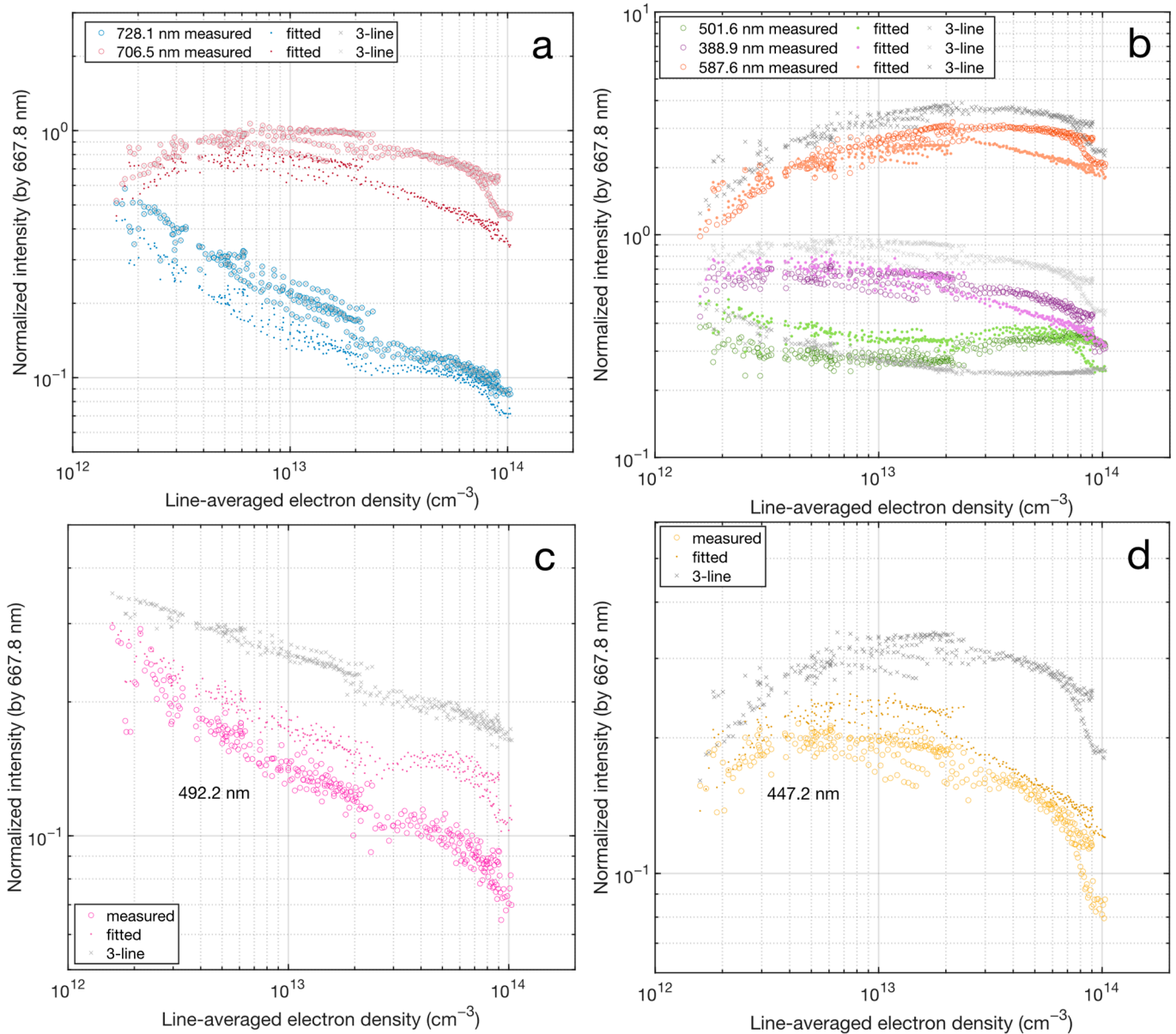


Figure 9. Comparison of the normalized intensity (colored dots and circles represent the measured line intensity and line intensity obtained using the novel model, respectively, and the crosses represent the line intensity obtained using the three-line method). (a) Comparison of the 706.5 nm and 728.1 nm lines. (b) Comparison of the 388.9 nm, 501.6 nm, and 587.6 nm lines. (c) Comparison of the 492.2 nm line. (d) Comparison of the 447.2 nm line.

Figure 11 shows the escape factors obtained by fitting. The escape factors for all three states exhibited similar trends, with an increase in the line-averaged electron density. State 2¹P had the smallest escape factor, which decreased from approximately 0.6 to 0.005 when the line-averaged electron density was lower than $6 \times 10^{13} \text{ cm}^{-3}$. Then, it increased to approximately 0.02 at 10^{14} cm^{-3} . State 4¹P had the largest escape factor in the range of 0.07–0.9. The escape factor for state 3¹P was between those for states 2¹P and 4¹P (0.03–0.8). This is a reasonable result because the reabsorption rate is proportional to the Einstein A coefficient, which decreases with an increase in the principal quantum number of the upper level. In the low line-averaged electron density region, the fitted escape factors are restricted by the calculated ones, which are functions of N_1 . Because N_1 increased with increasing line-averaged electron density, the reabsorption rate increased and the escape factors showed decreasing trends. The increase in the escape factor in the high

line-averaged electron density region could be due to a decrease in atom densities. The intensities of all measured lines decreased in the high line-averaged electron density region, which is consistent with the behavior of the optical escape factor. The reason for the decrease in the line intensity in the high line-averaged density region is not yet clear and requires further study.

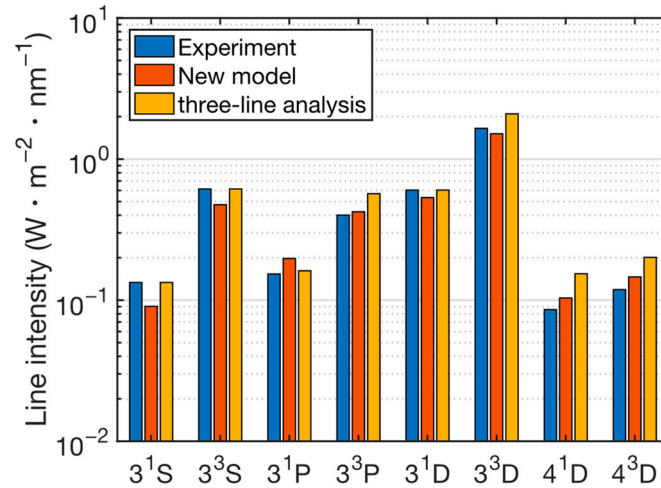


Figure 10. Comparison of line spectra obtained in experiments with counterparts reproduced by the new model and three-line analysis (line-averaged electron density: $\bar{n}_e = 2 \times 10^{13} \text{ cm}^{-3}$).

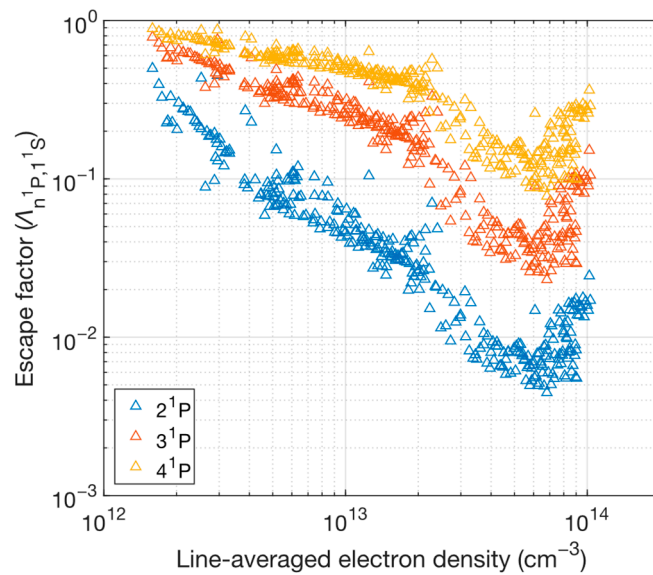


Figure 11. Escape factor fitted with the novel model (blue, orange, and yellow symbols represent the escape factor for transition from states 2^1P , 3^1P , and 4^1P to ground state 1^1S , respectively).

5. Conclusions

In this study, the helium CR model was modified by including an optical escape factor. An algorithm was developed to use n_e , T_e , n_1 , $\Lambda_{2^1P,1^1S}$, $\Lambda_{3^1P,1^1S}$, and $\Lambda_{4^1P,1^1S}$ to fit the eight emission lines in the visible wavelength range. According to the results, the algorithm can precisely diagnose the electron density and temperature of the LHD helium plasma. The disagreement of the line at 501.6 nm in the conventional three-line diagnosis can be solved by including the optical escape factor in the CR model and increasing the number of input lines from three to eight.

However, in the developed algorithm, the differences between the measured and fitted results of states 3^1S , 3^3S , and 3^1D increased slightly compared to the conventional method.

This can be improved by including the statistical weights of the object functions. In general, the algorithm performs well in determining the electron density and temperature.

The algorithm provides another option to diagnose the electron density and temperature of low-pressure helium plasma using the OES method, and it can be applied to the plasma under various conditions. The validity of the algorithm for other types of helium plasmas will be investigated in the future.

Author Contributions: Conceptualization, K.L., M.G. and H.A.; methodology, K.L. and M.G.; software, K.L.; investigation, M.G.; resources, M.G.; writing—original draft preparation, K.L. and M.G.; writing—review and editing, K.L. and M.G.; supervision, H.A.; project administration, H.A.; funding acquisition, H.A. All authors have read and agreed to the published version of the manuscript.

Funding: This research received no external funding.

Institutional Review Board Statement: Not applicable.

Informed Consent Statement: Not applicable.

Data Availability Statement: Not applicable.

Conflicts of Interest: The authors declare no conflict of interest.

References

1. Lin, K.; Nezu, A.; Akatsuka, H. Optical emission spectroscopy diagnosis of low-pressure microwave discharge helium plasma based on collisional-radiative model. *Jpn. J. Appl. Phys.* **2022**, *61*, 116001. [[CrossRef](#)]
2. Yuji, T.; Fujii, S.; Mungkung, N.; Akatsuka, H. Optical emission characteristics of atmospheric-pressure nonequilibrium microwave discharge and high-frequency DC pulse discharge plasma jets. *IEEE Trans. Plasma Sci.* **2009**, *37*, 839–845. [[CrossRef](#)]
3. Goto, M.; Morita, S. Determination of the hydrogen and helium ion densities in the initial and final stages of a plasma in the Large Helical Device by optical spectroscopy. *Phys. Plasmas* **2003**, *10*, 1402. [[CrossRef](#)]
4. Onishi, H.; Yamazaki, F.; Hakozaiki, Y.; Takemura, M.; Nezu, A.; Akatsuka, H. Measurement of electron temperature and density of atmospheric-pressure non-equilibrium argon plasma examined with optical emission spectroscopy. *Jpn. J. Appl. Phys.* **2021**, *60*, 026002. [[CrossRef](#)]
5. Sawada, K.; Yamada, Y.; Miyachika, T.; Ezumi, N.; Iwamae, A.; Goto, M. Collisional-radiative model for spectroscopic diagnostic of optically thick helium plasma. *Plasma Fusion Res.* **2010**, *5*, 001. [[CrossRef](#)]
6. Kajita, S.; Suzuki, K.; Tanaka, H.; Ohno, N. Helium line emission spectroscopy in recombining detached plasmas. *Phys. Plasmas* **2018**, *25*, 063303. [[CrossRef](#)]
7. Lee, W.; Oh, C. Optical diagnostics of helium recombining plasmas with collisional radiative model. *Phys. Plasmas* **2018**, *25*, 113504. [[CrossRef](#)]
8. Nishijima, D.; Hollmann, E.M. Determination of the optical escape factor in the He I line intensity ratio technique applied for weakly ionized plasmas. *Plasma Phys. Control. Fusion* **2007**, *49*, 791. [[CrossRef](#)]
9. Goto, M. Collisional-radiative model for neutral helium in plasma revisited. *J. Quant. Spectrosc. Radiat. Transf.* **2003**, *76*, 331–344. [[CrossRef](#)]
10. Fujimoto, T. A collisional-radiative model for helium and its application to a discharge plasma. *J. Quant. Spectrosc. Radiat. Transfer* **1979**, *21*, 439–455. [[CrossRef](#)]
11. Ralchnko, Y.V.; Janev, R.K.; Kato, T.; Fursa, D.V.; Bray, I.; Heer, F.J.D. *Cross Section Database for Collisional Processes of Helium Atom with Charged Particles. I. Electron Impact Processes*; Rep. NIFS-DATA-59 2000; NISF: Nagoya, Japan, 2000.
12. Shah, M.B.; Elliott, D.S.; McCallion, P.; Gilbody, H.B. Single and double ionisation of helium by electron impact. *J. Phys. B* **1988**, *21*, 2751–2761. [[CrossRef](#)]
13. Fujimoto, T. *Semi-Empirical Cross Section and Rate Coefficients for Excitation and Ionization by Electron Collision and Photoionization of Helium*; Rep. IPP-AM-8 1978; Institute of Nagoya Physics, Nagoya University: Nagoya, Japan, 1978.
14. Goto, M.; Fujimoto, T. *Collisional-Radiative Model for Neutral Helium in Plasma: Excitation Cross Section and Singlet-Triplet Wave-Function Mixing*; Rep. NIFS-DATA-43 1997; NISF: Nagoya, Japan, 1997.
15. Goto, M.; Morita, S. Determination of the line emission locations in a large helical device on the basis of the Zeeman effect. *Phys. Rev. E* **2002**, *65*, 026401. [[CrossRef](#)]
16. Schweer, B.; Mank, G.; Pospieszczyk, A.; Brosda, B.; Pohlmeier, B. Electron temperature and electron density profiles measured with a thermal He-beam in the plasma boundary of TEXTOR. *J. Nucl. Mater.* **1992**, *196–198*, 174–178. [[CrossRef](#)]
17. Goto, M.; Sawada, K. Determination of electron temperature and density at plasma edge in the Large Helical Device with opacity-incorporated helium collisional-radiative model. *J. Quant. Spectrosc. Radiat. Transf.* **2014**, *137*, 23–28. [[CrossRef](#)]
18. Kajita, S.; Ohno, N. Practical selection of emission lines of He I to determine the photon absorption rate. *Rev. Sci. Instrum.* **2011**, *82*, 023501. [[CrossRef](#)] [[PubMed](#)]

19. Iida, Y.; Kado, S.; Tanaka, S. Calculation of spatial distribution of optical escape factor and its application to He I collisional-radiative model. *Phys. Plasmas* **2010**, *17*, 123301.
20. Irons, F.E. The escape factor in plasma spectroscopy-I. the escape factor defined and evaluated. *J. Quant. Spectrosc. Radiat. Transf.* **1979**, *22*, 1–20. [[CrossRef](#)]
21. Fujimoto, T. *Plasma Spectroscopy*; Clarendon Press: Oxford, UK, 2004.
22. Akatsuka, H.; Suzuki, M. Numerical study on population inversion and lasing conditions in an optically thick recombining helium plasma. *Contrib. Plasma Phys.* **1994**, *34*, 539–561. [[CrossRef](#)]
23. Kim, S.; Koh, K.; Lustig, M.; Boyd, S.; Gorinevsky, D. An interior-point method for large-scale l_1 -regularized least squares. *IEEE J. Sel. Top. Signal Process.* **2007**, *1*, 606–617. [[CrossRef](#)]
24. Zhang, Y. Solving large-scale linear programs by interior-point methods under the Matlab Environment. *Optim. Methods Softw.* **1998**, *10*, 1–31. [[CrossRef](#)]
25. Rajasekhar Reddy, M.; Nithish Kumar, B.; Madhusudana Rao, N.; Karthikeyan, B. A new approach for bias–variance analysis using regularized linear regression. In *Advances in Bioinformatics, Multimedia, and Electronics Circuits and Signals*; Springer: Singapore, 2020.
26. Wilson, R.C.; Hancock, E. Bias-variance analysis for controlling adaptive surface meshes. *Comput. Vis. Image Underst.* **2000**, *77*, 25–47. [[CrossRef](#)]
27. Doroudi, S. The bias-variance tradeoff: How data science can inform educational debates. *AERA Open* **2020**, *6*, 1–18. [[CrossRef](#)]

Disclaimer/Publisher’s Note: The statements, opinions and data contained in all publications are solely those of the individual author(s) and contributor(s) and not of MDPI and/or the editor(s). MDPI and/or the editor(s) disclaim responsibility for any injury to people or property resulting from any ideas, methods, instructions or products referred to in the content.